APL Materials

RESEARCH ARTICLE | NOVEMBER 27 2023

# Reliably straining suspended van der Waals heterostructures

Daniele Nazzari ; Jakob Genser; Masiar Sistani ; Maximilian G. Bartmann ; Xavier Cartoixà; Riccardo Rurali ; Walter M. Weber ; Alois Lugstein

Check for updates

*APL Mater.* 11, 111123 (2023)
https://doi.org/10.1063/5.0166460

View Online
Export Citation
CrossMark

11 January 2024 11:49:08

AIP Advances
Why Publish With Us?
25 DAYS average time to 1st decision
740+ DOWNLOADS average per article
INCLUSIVE scope
Learn More
AIP Publishing

AIP Publishing

APL Materials ARTICLE pubs.aip.org/aip/apm

# Reliably straining suspended van der Waals heterostructures

Cite as: APL Mater. 11, 111123 (2023); doi: 10.1063/5.0166460
Submitted: 5 July 2023 • Accepted: 2 November 2023 •
Published Online: 27 November 2023

View Online Export Citation CrossMark

Daniele Nazzari,[1,a)] Jakob Genser,[1] Masiar Sistani,[1] Maximilian G. Bartmann,[1] Xavier Cartoixà,[2] Riccardo Rurali,[3] Walter M. Weber,[1] and Alois Lugstein[1]

## AFFILIATIONS

[1] Institute of Solid State Electronics, Technische Universität Wien, Gußhausstraße 25-25a, 1040 Wien, Austria
[2] Departament d'Enginyeria Electrònica, Universitat Autònoma de Barcelona, 08193 Bellaterra, Barcelona, Spain
[3] Institut de Ciència de Materials de Barcelona, ICMAB-CSIC, Campus UAB, 08193 Bellaterra, Spain

[a)] **Author to whom correspondence should be addressed:** daniele.nazzari@tuwien.ac.at

## ABSTRACT

2D materials provide a rapidly expanding platform for the observation of novel physical phenomena and for the realization of cutting-edge optoelectronic devices. In addition to their peculiar individual characteristics, 2D materials can be stacked into complex van der Waals heterostructures, greatly expanding their potential. Moreover, thanks to their excellent stretchability, strain can be used as a powerful control knob to tune or boost many of their properties. Here, we present a novel method to reliably and repeatedly apply a high uniaxial tensile strain to suspended van der Waals heterostructures. The reported device is engineered starting from a silicon-on-insulator substrate, allowing for the realization of suspended silicon beams that can amplify the applied strain. The strain module functionality is demonstrated using single- and double-layer graphene layers stacked with a multilayered hexagonal boron nitride flake. The heterostructures can be uniaxially strained, respectively, up to ~1.2% and ~1.8%.

*© 2023 Author(s). All article content, except where otherwise noted, is licensed under a Creative Commons Attribution (CC BY) license (http://creativecommons.org/licenses/by/4.0/).* https://doi.org/10.1063/5.0166460

11 January 2024 11:49:08

## I. INTRODUCTION

The discovery and synthesis of many 2D materials have equipped researchers with a large variety of options for the realization of novel optoelectronic devices. Many of these materials are predicted to possess highly desirable electrical, optical, and mechanical properties. In particular, 2D materials are extremely flexible and can withstand enormous elastic deformations without displaying any plasticity. This offers a powerful control knob over many properties of the 2D materials, as strain can be a very effective way to tune and improve the optical, electrical, and thermal responses. For example, strain can be successfully employed to open a bandgap in graphene[1] or to tune the electronic properties of semiconducting transition metal dichalcogenides (TMDs),[2–5] but also to vary the charge carrier effective masses,[6] the thermal conductivity,[7,8] the dielectric properties,[6] and the spin–orbit coupling.[9,10] Many methods for applying strain to 2D materials have been proposed and realized experimentally. A simple but effective technique requires the pre-patterning of a substrate to form holes, trenches, or hills. 2D materials are then deposited on top of these structures, and inhomogeneous strain arises as an effect of the relaxation of the 2D flakes on top of the hills and trenches;[10] in this case, the strain level is very low and fixed. The deformation can be vastly increased by the application of an external load on a 2D flake suspended over a hole or a trench by using an AFM cantilever.[11] Another method for creating strain gradients is based on the formation of wrinkles.[12] Yet, a different approach is needed in order to uniformly and precisely strain a 2D material. A successful technique relies on the interaction that is formed between the 2D flake and a flexible substrate; through the deformation of the substrate, it is possible to transfer a certain level of strain to the 2D material.[13–18] These approaches require the 2D material to be in direct contact with the flexible substrate in order to transfer strain. However, extrinsic scattering arising from the interaction with the substrate can result in a degradation of the electrical properties of the 2D material.[19] This problem can be solved by suspending the strained flake or by encapsulating it with insulating van der Waals materials, such as hexagonal boron nitride (hBN).[20] Suspended graphene was successfully strained up


© Author(s) 2023

to 1% using comb-drive actuators,[21] but the fabrication process is highly complex and requires an electron beam lithography step. Here, we present a novel method for applying uniaxial tensile strain to suspended and encapsulated 2D materials using micromechanical straining devices (MSDs), which we have previously shown to be able to uniaxially strain Ge nanowires up to ~5%.[22] For demonstration purposes, we investigated the application of tensile strain to suspended single- and double-layer graphene flakes. By comparing the Raman signature to simulated spectra, we show that the 2D materials can be strained uniformly and uniaxially up to ~1.8% in a reproducible way.

## II. DISCUSSION

The MSD fabrication process, shown in panels (a)–(h) in Fig. 1, starts with a silicon-on-insulator (SOI) substrate with a handle wafer thickness of 500 $\mu$m, a device layer (DL) thickness of 3 $\mu$m, and a 1 $\mu$m thick buried oxide (BOX) layer. A trench with a width of ~1.5 $\mu$m is patterned using optical lithography, followed by reactive ion etching (RIE); see Figs. 1(b) and 1(c). Subsequently, the BOX is etched using buffered hydrofluoric acid (BHF). The sample is kept in the BHF for a prolonged time until the BHF diffuses under the device layer and under-etches the oxide by ~120 $\mu$m, forming two freestanding Si beams [Fig. 1(d)]. Then, to electrically isolate the two beams, 300 nm thick $SiO_2$ is grown through a wet thermal oxidation process [Fig. 1(e)]. This reduces the width of the trench down to 1 $\mu$m. Once this step is completed, the flake to be strained can be transferred onto the device. This is achieved by recurring to a dry-viscoelastic transfer method, where a polymer-based stamp is used to pick up 2D materials through a temperature-assisted process.[23,24] Here, we rely on a polymeric stamp composed of polypropylene carbonate (PPC) and polydimethylsiloxane (PDMS), fixed on a glass

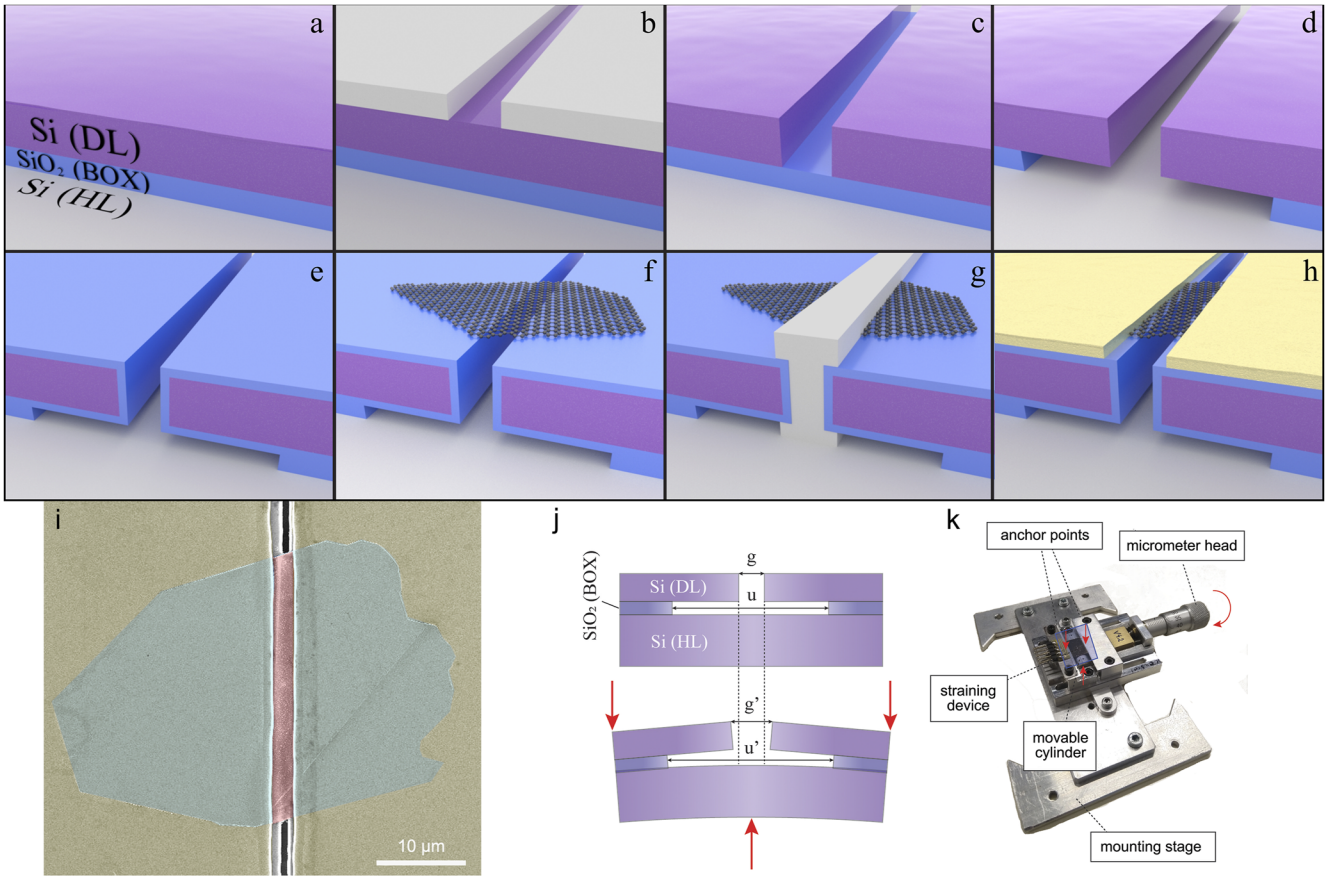


**FIG. 1.** Schematic representation of all the process steps required for the fabrication of the strain device: (a) The starting substrate, a SOI wafer, is composed of a 3 $\mu$m thick Si device layer (purple) on a 1 $\mu$m thick BOX (blue). The handle Si layer (gray) is 500 $\mu$m thick. (b) Resist is added to the wafer and patterned through optical lithography. (c) A trench is etched using RIE until the BOX is reached. (d) The BOX is under-etched using a BHF-based wet process. (e) The resulting beams are passivated by a thermally grown, 300 nm-thick $SiO_2$ layer. (f) The target 2D flake is transferred onto the strain device. (g) Resist is added and patterned through optical lithography. (h) A Ti/Au metallic layer is evaporated onto the sample. After lift-off, the flake is pinned down onto the strain device, with the exposed portion being positioned on the trench. (i) An optical microscope image showing the result of the previous steps (a)–(h). The false colors show the position of the metallic layer (yellow), pinning down the flake (blue). In red, the exposed part of the flake is located across the trench. (j) A schematic representation of how strain is applied to the flake. Utilizing a three point method, pressure is applied at the locations indicated by the red arrows. The under-etched region allows us to multiply the intensity of the applied strain. (k) Photography showing the mounting stage. The chip is mounted in the center and anchored under the two specified points. By rotating the micrometer head, the cylinder is moved, increasing the strain applied to the sample.

11 January 2024 11:49:08


© Author(s) 2023

slide by Scotch tape. The glass slide is then attached to a micromanipulator, allowing precise positioning of the transfer stamp. A flake of multilayer hexagonal boron nitride (hBN) is first picked up using the polymeric stamp. This hBN flake serves as a contact layer for the target 2D layer, which can be picked up while ensuring the best possible encapsulation.

In this work, we have investigated the uniaxial tensile straining of suspended single-layer and double-layer graphene flakes. The choice of using graphene for testing this new strain approach is well supported by the fact that this material has intensively been investigated in the past, providing useful information for the determination of the effectively applied deformation.[25] The stack formed by the 2D layer and its hBN carrier is then deposited across the trench of the straining device [Fig. 1(f)]. Once released over the trench, the stack is able to relax. The thicker hBN flake, thanks to its rigidity, prevents the 2D layer from hanging down into the trench. After positioning the flake, the trench is filled using LOR3A resist, and, afterward, an additional AZ5214 resist layer is spun on top of the device. The resist is patterned through photolithography, obtaining a resist layer that covers the suspended part of the flake [Fig. 1(g)]. Finally, a 5 nm thick Ti adhesion layer, followed by a 200 nm thick Au layer, is evaporated on top of the device. The metal layer has the role of fixing the stack during strain through friction. At the end of the lift-off process [Fig. 1(h)], the stack is fixed on top of the trench, ready to be strained. A false-color SEM image of the final device can be seen in Fig. 1(i), where a single-layer graphene flake covered by a multilayer hBN flake is positioned over the trench and pinned down by the evaporated metallic layer. The region of the stack that will be strained is evidenced in red, while the area covered and fixed by the metallic layer is highlighted in blue. Once the sample is completed, it can be inserted into a three-point bending device. In this way, pressure can be applied at the two sides of the MSD as well as from the backside, as shown by the red arrows in Fig. 1(j). As calculated previously,[22] the strain that is generated into the top surface of the SOI layer is increased by a factor $\frac{u}{g}$, where $g$ is the trench width and u is the under-etch length. The maximum strain level that can be theoretically achieved in the gap region by this strain device is up to 36%. In practice, once the strain level reaches either the rupture point of the strained material or the maximum force that can be sustained by the fixing metal layer, the strain device will fail, thus limiting the maximum strain. Additional photos of the realized strain devices and a more detailed description of how strain is applied to the target material can be found in the supplementary material.

The final device is then moved under a confocal $\mu$-Raman spectroscopy setup. Here, the laser beam is focused on the suspended part of the flake, effectively measuring the Raman response while the target material gets stretched. The strain can be applied and increased by rotating the micrometer head. Initially, a single-layer graphene flake is chosen as the target. This choice is based on the fact that the effect of strain on the optical phonon modes in graphene has been intensively investigated,[25] allowing us to easily assess the performance of the strain device directly using Raman spectroscopy. In order to measure the applied strain, we focus on the G peak of graphene, which corresponds to the doubly degenerate $E_{2G}$ phonon at the center of the Brillouin zone and has a frequency $\omega_{G_0} = 1590$ cm$^{-1}$ for an unstrained layer. The degeneracy is lifted with the application of uniaxial strain to the graphene layer due to the asymmetry of the deformation. Therefore, two peaks can be observed, $G^+$ and $G^-$, with a Raman frequency of, respectively, $\omega_{G_+}$ and $\omega_{G_-}$, in accordance with the previously used nomenclature.[25] By calculating the spectral shift of the $G^+$ and $G^-$ peaks with respect to the unstrained peak—i.e., $\Delta\omega_{G_\pm} = \omega_{G_\pm} - \omega_{G_0}$—it is possible to retrieve the applied strain,

$$\Delta\omega_{G_\pm} = -\omega_{G_0}\gamma_{G_0}(1-\nu)\varepsilon \pm \frac{1}{2}\beta_{G_0}\omega_{G_0}(1+\nu)\varepsilon,$$

where

$$\gamma_{G_0} = -\frac{1}{\omega_{G_0}}\frac{\partial\omega^h_{G_0}}{\partial\varepsilon_h}$$

and

$$\beta_{G_0} = \frac{1}{\omega_{G_0}}\frac{\partial\omega^s_{G_0}}{\partial\varepsilon_s}$$

with $\varepsilon_h$ and $\varepsilon_s$ indicating, respectively, the hydrostatic and shear components of the applied strain, $\gamma_{G_0}$ is the Grüneisen parameter for the $E_{2G}$ phonon mode, $\beta_{G_0}$ is the shear deformation potential, $\omega_{G_0}$ is the position of the G peak for the unstrained layer, and $\nu$ is the Poisson's ratio of the strained material. For a freestanding graphene layer, all these parameters are reported in the literature.[25,26] Notice, however, that in the present work, graphene is in contact with the handling hBN layer. This might alter the observed shift of the Raman peaks for a certain strain, as the Poisson ratio is influenced by the mechanical properties of the handling layer. The Raman spectra observed for different strain levels are shown in Fig. 2(a). As expected, the G mode is separated into the $G^+$ and $G^-$ components. The spectra are fitted using the Lorentzian function, as indicated by the shadowed areas in the figure, allowing us to obtain the position of the peaks. Considering the quantity

$$\frac{\Delta\omega_{G_+} + \Delta\omega_{G_-}}{\Delta\omega_{G_+} - \Delta\omega_{G_-}} = -\frac{2\gamma_{G_0}}{\beta_{G_0}}\frac{(1-\nu)}{(1+\nu)},$$

we can extract the observed Poisson ratio, as this quantity is independent of the applied strain. From this, we obtain $\nu = 0.28 \pm 0.045$. This seemingly unnatural result, larger than both $\nu_{hBN} = 0.211$ and $\nu_{graphene} = 0.165$,[27] is, however, statistically compatible with the former value while clearly deviating from the latter one. This indicates that the hBN handling layer has a non-negligible effect on the strain behavior of the graphene layer. To account for the effect of the hBN layer, we carry out first-principles calculations of the Raman spectra of single-layer graphene under the application of uniaxial tensile strain in the freestanding case [Fig. 2(b)] and assuming perfect contact with a hBN monolayer [Fig. 2(c)]. From our results, it can be clearly seen that the peak divergence is less pronounced for the hBN/graphene stack. Based on the previously reported observation that the hBN is influencing the strain behavior of the graphene layer, we use the parameters reported in Fig. 2(c) to extract the applied strain, thereby assuming a shift of $-12.6 \pm 0.6\%^{-1}$ cm$^{-1}$ for the $G^-$ peak and of $-34.1 \pm 0.6\%^{-1}$ cm$^{-1}$ for the $G^+$ peak. The peak positions are finally plotted with respect to the extracted strain in Fig. 2(d), showing that the graphene flake can be strained up to 1.2%.

A similar approach is then followed in the case of bilayer graphene. The target flake is identified using Raman spectroscopy

11 January 2024 11:49:08


© Author(s) 2023

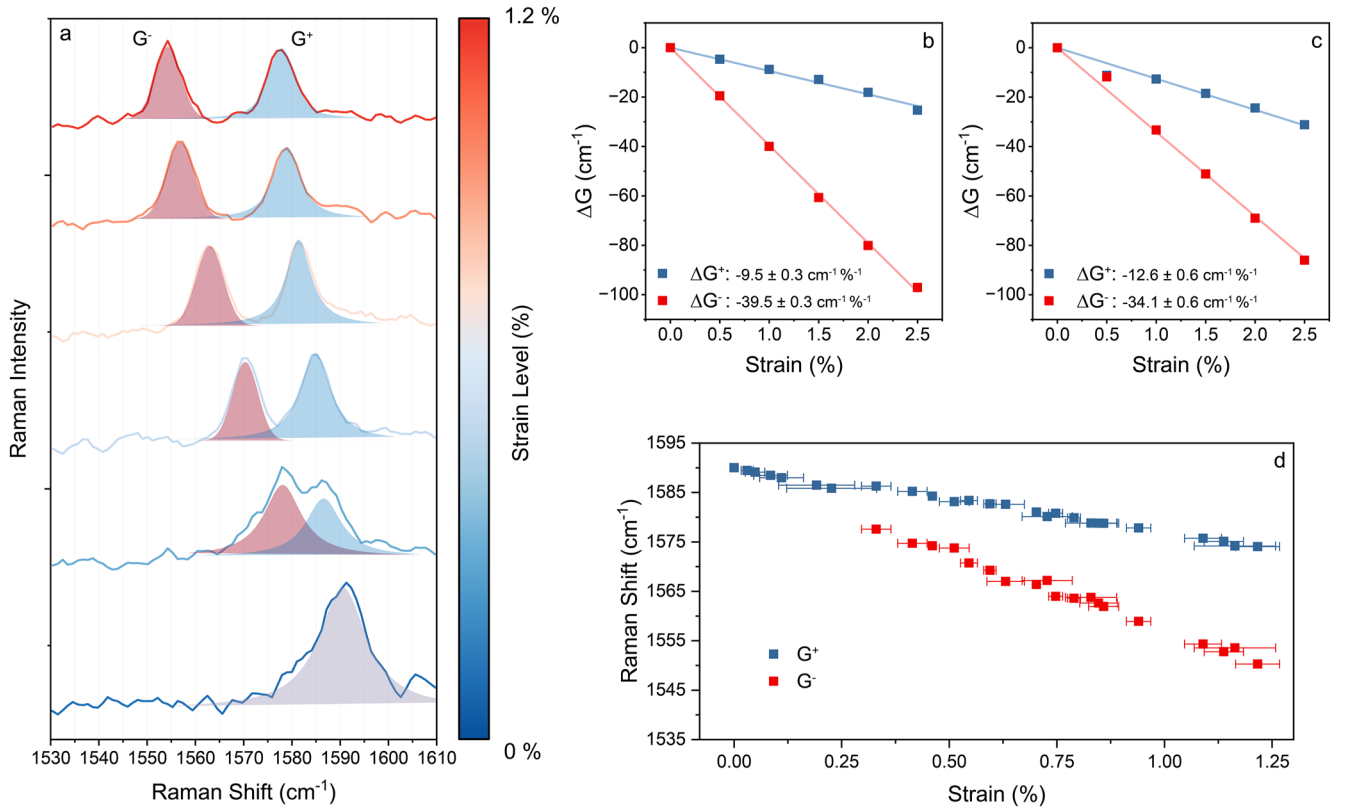


**FIG. 2.** A single layer graphene flake is placed across the trench using an hBN flake as the handling layer. (a) Raman spectra collected upon application of tensile strain to the graphene flake. The examined spectral region is focused on the G peak, which subdivides into $G^+$ and $G^-$ upon strain application. The strain is estimated using the $G^+$ and $G^-$ positions and the parameters extrapolated from simulations. (b) and (c) First-principles calculations of the position of the $G^+$ and $G^-$ peaks for a single layer graphene in, respectively, a freestanding configuration and when in contact with an hBN flake. (d) Position of the Raman peaks in relation to the estimated strain values, showing a maximum applied strain of ~1.2%.

and transferred to the strain device following the same procedure used for the single layer flake. Once fixed, bilayer graphene can be strained by increasing the gap width of the strain device. As before, Raman spectroscopy is used to precisely determine the applied strain by comparing the G peak shift and split with first-principles calculations, as shown in Figs. 3(a) and 3(b). Remarkably, after applying an initial strain level of 1.2%, a third G peak, defined here as $G^*$, can be observed appearing in the Raman spectrum. The position of the new peak is then stable upon further increases in the applied strain. Clearly, the position of $G^*$ is close to the one observed for unstrained single-layer graphene, implying that one of the two layers composing the flake has relaxed into the unstrained configuration, while the other is kept strained. Once the strain device is relaxed, the three peaks move back to the starting configuration, showing that all layers are once again unstrained. When the strain is further applied, the two layers are still able to be separated, with one remaining relaxed while the second being strained. In order to correctly estimate the applied strain, one has to take into consideration that, after the appearance of the $G^*$ peak, only one layer is actively strained. For this reason, the strain values shown in Fig. 3 are obtained using the parameters estimated for a bilayer graphene flake upon the appearance of the $G^*$ peak, while the single-layer graphene parameters are used thereafter. It is important to note that with this device, one can freely move and stretch one layer of graphene next to an unstrained one, thereby allowing one to tune the degree of lattice mismatch. This enables the realization of a Moiré superlattice, potentially using any kind of multilayered van der Waals material, a construct that has been shown to hold exotic electrical, optical, and magnetic properties.[28–31]

The strain estimation has been based entirely on the analysis of the Raman spectra of the single- and double-layer graphene flakes. Nevertheless, the hBN handling layer is also subjected to a tensile strain. Figure S1 shows the hBN $E_{2g}$ Raman spectra for the unstrained and maximally strained configurations. In the latter case, an additional shoulder is observable on the left hand side of the $E_{2g}$ peak. By fitting the spectrum with a dual-peak model, the main peak is found to be centered at 1365.02 ± 0.03 $cm^{-1}$, in accordance with the value expected for an unstrained multilayer hBN flake.[32] The position of the additional shoulder is estimated to be ~1337 ± 1 $cm^{-1}$, resulting in a shift of ~−28 $cm^{-1}$. This result is compatible with an applied tensile strain of ~1.87% for a multilayer hBN flake,[33] a very similar value to the one estimated for the graphene

11 January 2024 11:49:08


© Author(s) 2023

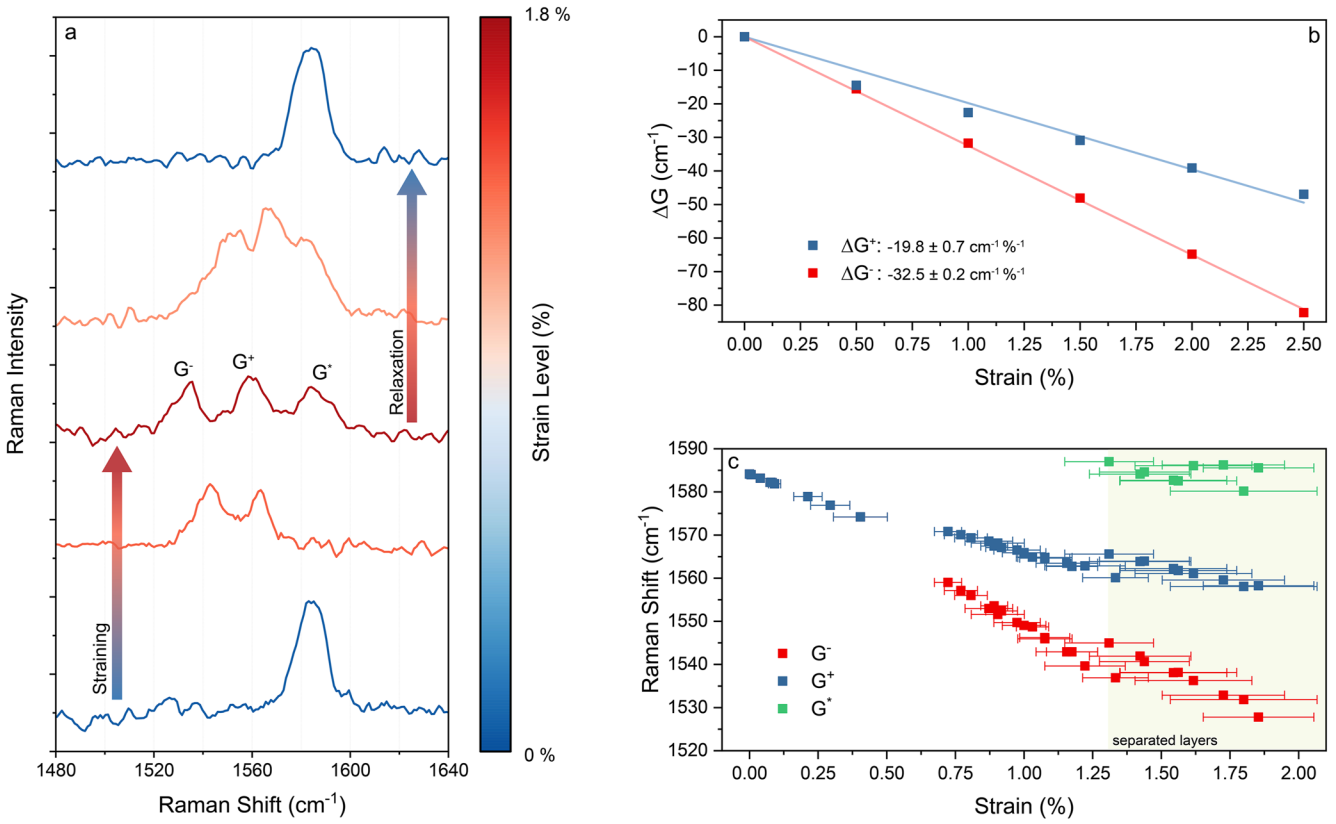


**FIG. 3.** A double layer graphene flake is placed on the strain device. (a) Raman spectra collected upon application of tensile strain to the target flake. It is possible to observe, initially, the splitting of the G peak, similarly to Fig. 2. When the strain surpasses ~1.2%, a new peak ($G^*$) appears. The strain value is calculated by comparing the measured peak shift to data extracted from first-principles calculations, as shown in (b). (c) Position of the Raman peaks in relation to the estimated strain values. The position of the $G^*$ peak is stable upon strain increase. The maximum applied strain is ~1.8%.

layer. This result confirms the validity of the strain values obtained from the analysis of the graphene Raman spectra. At the same time, it shows that tensile strain can be transferred to the encapsulating hBN layer, proving the capability of the device to strain a van der Waals stack. However, it must be noted that the hBN layer is much thicker than the target graphene. Only a certain number of hBN layers can be successfully strained, as certified by the appearance of the shoulder in the Raman signal, while the others remain relaxed, giving rise to the unshifted $E_{2g}$ peak.

It must be noted that the maximum achieved strain is well below the theoretical maximum that could be obtained using the described straining device, as the same architecture was able to generate up to ~5% tensile strain in Ge nanowires.[22] This shows that the limiting factor is represented by the capability of pinning the 2D flake on top of the straining device when stretched. Ultimately, it can be assumed that the flake is slipping away from the metallic contacts, resulting in the failure of the device. A possible solution would be to change the contact material in order to achieve a better grip between the 2D flake and the strain device. Alternatively, nanoholes can be milled into the 2D flake using a focused ion beam,[34] leading to the realization of a much stronger contact between the metallic layer and the target 2D material. When comparing the results obtained here with other strain experiments reported in the literature, as summarized in Table 1 (see the supplementary material), it is noticeable that higher strain levels can be obtained recurring to methods based on flexible substrates by reducing the slippage of the 2D flakes through, for example, an innovative method using adamantane coating.[18] As discussed earlier, further improvements to our design could reduce the slippage of the flakes, improving the maximum achievable strain. Nevertheless, it must be clear that the main advantage of the technique discussed in this work is represented by the ability to strain suspended flakes, thereby avoiding any contact with a substrate. This is fundamental for extracting the best performances from a 2D material-based device, as the interaction with a substrate can induce unwanted doping[35] or changes to the bandstructure[36] as well as introduce traps and defects that strongly affect the charge transport behavior.[19] It is worth noting that the method proposed here is compatible with any 2D materials that can be exfoliated and transferred. In addition, by coating the suspended beams of the strain chip with a metallic layer, thus ensuring an electrical contact between the 2D flake and the pads, it will be possible to measure the electrical transport across the strained 2D materials,

11 January 2024 11:49:08


© Author(s) 2023

similarly to what has been done for nanowires.[22] This method has a great potential for enabling a deeper investigation of the effects of strain in a variety of suspended 2D flakes, where strain has already been proven to tune the material properties, such as TMDs, which have shown a high sensitivity toward deformations,[37] as well as black phosphorous[38] and materials of the MXene family[39] or of the Xene family.[40] Possible future applications of the platform are the study of carrier mobility enhancement through the application of strain as well as the realization of strain-tunable photodetectors, following what has been done with $MoS_2$,[17,41] with the advantage of working with a suspended material, unperturbed by the interaction with the substrate.

## III. CONCLUSION

We have here demonstrated the realization of a straining device that can be used to strain 2D materials with an arbitrary number of layers up to ~1.8% in a reproducible way. The applied strain is tracked using confocal $\mu$-Raman spectroscopy, as the collected spectrum is strongly affected by the lattice changes induced by the strain. The realized device has the capability of straining freestanding 2D layers without the request of a flexible substrate to induce the deformation. With minimal updates, this method will also enable the measurement of electrical transport in strained 2D layers. In addition, we have demonstrated that this approach also enables us to strain only one layer of a bilayer graphene flake, possibly enabling the realization of lattice mismatch-induced Moiré superlattices, a platform that could enable the observation of exotic physical properties.

## IV. METHODS

### A. Strain device fabrication

Silicon-on-insulator (SOI) substrates characterized by a 500 $\mu$m thick handle layer (HL), a 3 $\mu$m thick device layer (DL), and a 1 $\mu$m thick buried-oxide (BOX) are used. The substrate is initially cleaned using a combination of acetone and isopropanol baths, deionized water rinsing, and a final oxygen plasma treatment. Trenches with a width of ~1 $\mu$m are patterned by optical lithography into a layer of AZ5214E positive resist. The exposed areas are etched away using an Oxford Instruments RIE ICP-65, using an $SF_6/O_2$-based process, at a temperature of −108°. An interferometer signal allows us to stop the etching process as soon as the BOX layer is reached. The BOX is etched starting from the trenches using 40% diluted hydrofluoric acid (HF), defining the two suspended beams. The Si beams are partially oxidized in an ATV PEO-601 furnace. The target 2D material is moved to the trench using a dry-transfer technique based on a PDMS/PPC stamp after filling the trenches with a mixture of LOR3A and AZ5214E resist. After a final lithography step, a 5 nm thick Ti layer, followed by a 200 nm thick Au layer, is deposited using a Plassys MEB 550S evaporator.

### B. Raman spectroscopy

All the Raman spectra are acquired using a confocal $\mu$-Raman setup (WITec Alpha 300) in backscattering geometry, equipped with a Zeiss 100× objective (NA = 0.75, WD = 4 mm). A frequency doubled Nd:YAG laser ($\lambda$ = 532 nm) is used as an excitation source. The beam is focused down to a diffraction-limited spot size of ~720 nm and centered to the suspended part of the flake. The laser power is adjusted in order to minimize heating effects. The acquired spectra are smoothed using a Savitzky–Golay filter and fitted using Lorentzian functions after linear background removal.

### C. First-principles calculations

Density-functional theory (DFT) calculations were performed with the ABINIT code,[42,43] using the Local Density Approximation (LDA) for the exchange–correlation energy, a plane-wave cutoff of 46 Ha, and norm-conserving pseudopotentials. The four- and eight-atom unit cells of graphene and bilayer graphene were sampled with a 26 × 45 grid of **k**-points. The optical phonon frequencies were obtained within density-functional perturbation theory (DFPT).[44] With this computational setup, we obtain frequencies of the Raman active phonon modes for unstrained bilayer graphene of 890 and 1604 $cm^{-1}$.

## SUPPLEMENTARY MATERIAL

See the supplementary material for an additional Raman spectrum of the hBN layer, a table of comparison between this work and select publications, and additional images of the realized strain device.

## ACKNOWLEDGMENTS

This work was funded by the Austrian Science Fund (FWF), Project No. P29244-N27. We thank the center for micro- and nanostructures (ZMNS) at the TU Vienna for access to the cleanroom facilities. R.R. acknowledges the financial support by MCIN/AEI/10.13039/501100011033 under Grant No. PID2020-119777GB-I00 and the Severo Ochoa Centers of Excellence Program under Grant No. CEX2019-000917-S and by the Generalitat de Catalunya under Grant No. 2021 SGR 01519. X.C. acknowledges the financial support by Spain's Ministerio de Ciencia Innovación y Universidades under Grant No. RTI2018-097876-B-C21 (MICIU/AEI/FEDER UE) and the Ministerio de Ciencia e Innovación under Grant No. PID2021-127840NB-I00 (MICINN/AEI/UE). The authors thankfully acknowledge the computer resources, technical expertise, and assistance provided by CESGA.

## AUTHOR DECLARATIONS

### Conflict of Interest

The authors have no conflicts to disclose.

### Author Contributions

**Daniele Nazzari**: Conceptualization (equal); Data curation (equal); Investigation (equal); Writing – original draft (equal). **Jakob Genser**: Conceptualization (equal); Data curation (equal); Investigation (equal); Writing – review & editing (equal). **Masiar Sistani**: Writing – review & editing (equal). **Maximilian G. Bartmann**: Writing – review & editing (equal). **Xavier Cartoixà**: Investigation (equal); Writing – review & editing (equal). **Riccardo Rurali**: Investigation (equal); Writing – review & editing (equal). **Walter M. Weber**: Funding acquisition (equal); Supervision (equal). **Alois Lugstein**:

11 January 2024 11:49:08


© Author(s) 2023

Conceptualization (equal); Data curation (equal); Funding acquisition (equal); Supervision (equal); Writing – review & editing (equal).

## DATA AVAILABILITY

The data that support the findings of this study are available from the corresponding author upon reasonable request.

## REFERENCES


[1] V. M. Pereira, A. H. Castro Neto, and N. M. R. Peres, Phys. Rev. B **80**, 045401 (2009).
[2] P. Johari and V. B. Shenoy, ACS Nano **6**, 5449 (2012).
[3] Q. Yue, J. Kang, Z. Shao, X. Zhang, S. Chang, G. Wang, S. Qin, and J. Li, Phys. Lett. A **376**, 1166 (2012).
[4] H. Shi, H. Pan, Y.-W. Zhang, and B. I. Yakobson, Phys. Rev. B **87**, 155304 (2013).
[5] P. Lu, X. Wu, W. Guo, and X. C. Zeng, Phys. Chem. Chem. Phys. **14**, 13035 (2012).
[6] A. Kumar and P. K. Ahluwalia, Physica B **419**, 66 (2013).
[7] S. Bhattacharyya, T. Pandey, and A. K. Singh, Nanotechnology **25**, 465701 (2014).
[8] L. Zhu, T. Zhang, Z. Sun, J. Li, G. Chen, and S. A. Yang, Nanotechnology **26**, 465707 (2015).
[9] H. Rostami, R. Roldán, E. Cappelluti, R. Asgari, and F. Guinea, Phys. Rev. B **92**, 195402 (2015).
[10] L. Mennel, M. M. Furchi, S. Wachter, M. Paur, D. K. Polyushkin, and T. Mueller, Nat. Commun. **9**, 516 (2018).
[11] S. Bertolazzi, J. Brivio, and A. Kis, ACS Nano **5**, 9703 (2011).
[12] A. Castellanos-Gomez, R. Roldán, E. Cappelluti, M. Buscema, F. Guinea, H. S. J. van der Zant, and G. A. Steele, Nano Lett. **13**, 5361 (2013).
[13] H. J. Conley, B. Wang, J. I. Ziegler, R. F. Haglund, S. T. Pantelides, and K. I. Bolotin, Nano Lett. **13**, 3626 (2013).
[14] C. R. Zhu, G. Wang, B. L. Liu, X. Marie, X. F. Qiao, X. Zhang, X. X. Wu, H. Fan, P. H. Tan, T. Amand, and B. Urbaszek, Phys. Rev. B **88**, 121301 (2013).
[15] S. B. Desai, G. Seol, J. S. Kang, H. Fang, C. Battaglia, R. Kapadia, J. W. Ager, J. Guo, and A. Javey, Nano Lett. **14**, 4592 (2014).
[16] Y. Wang, C. Cong, W. Yang, J. Shang, N. Peimyoo, Y. Chen, J. Kang, J. Wang, W. Huang, and T. Yu, Nano Res. **8**, 2562 (2015).
[17] P. Gant, P. Huang, D. Pérez de Lara, D. Guo, R. Frisenda, and A. Castellanos-Gomez, Mater. Today **27**, 8 (2019).
[18] F. Carrascoso, H. Li, J. M. Obrero-Perez, F. J. Aparicio, A. Borras, J. O. Island, A. Barranco, and A. Castellanos-Gomez, npj 2D Mater. Appl. **7**, 24 (2023).
[19] Y. Y. Illarionov, T. Knobloch, M. Jech, M. Lanza, D. Akinwande, M. I. Vexler, T. Mueller, M. C. Lemme, G. Fiori, F. Schwierz, and T. Grasser, Nat. Commun. **11**, 3385 (2020).
[20] X. Cui, G.-H. Lee, Y. D. Kim, G. Arefe, P. Y. Huang, C.-H. Lee, D. A. Chenet, X. Zhang, L. Wang, F. Ye, F. Pizzocchero, B. S. Jessen, K. Watanabe, T. Taniguchi, D. A. Muller, T. Low, P. Kim, and J. Hone, Nat. Nanotechnol. **10**, 534 (2015).
[21] M. Goldsche, G. J. Verbiest, T. Khodkov, J. Sonntag, N. von den Driesch, D. Buca, and C. Stampfer, Nanotechnology **29**, 375301 (2018).
[22] M. G. Bartmann, M. Sistani, S. Glassner, B. Salem, T. Baron, P. Gentile, J. Smoliner, and A. Lugstein, Nanotechnology **32**, 145711 (2021).
[23] F. Pizzocchero, L. Gammelgaard, B. S. Jessen, J. M. Caridad, L. Wang, J. Hone, P. Bøggild, and T. J. Booth, Nat. Commun. **7**, 11894 (2016).
[24] A. Castellanos-Gomez, M. Buscema, R. Molenaar, V. Singh, L. Janssen, H. S. J. van der Zant, and G. A. Steele, 2D Mater. **1**, 011002 (2014).
[25] T. M. G. Mohiuddin, A. Lombardo, R. R. Nair, A. Bonetti, G. Savini, R. Jalil, N. Bonini, D. M. Basko, C. Galiotis, N. Marzari, K. S. Novoselov, A. K. Geim, and A. C. Ferrari, Phys. Rev. B **79**, 205433 (2009).
[26] Y. C. Cheng, Z. Y. Zhu, G. S. Huang, and U. Schwingenschlögl, Phys. Rev. B **83**, 115449 (2011).
[27] A. Falin, Q. Cai, E. J. G. Santos, D. Scullion, D. Qian, R. Zhang, Z. Yang, S. Huang, K. Watanabe, T. Taniguchi, M. R. Barnett, Y. Chen, R. S. Ruoff, and L. H. Li, Nat. Commun. **8**, 15815 (2017).
[28] F. He, Y. Zhou, Z. Ye, S.-H. Cho, J. Jeong, X. Meng, and Y. Wang, ACS Nano **15**, 5944 (2021).
[29] Y. Xiao, J. Liu, and L. Fu, Matter **3**, 1142 (2020).
[30] K. Reidy, G. Varnavides, J. D. Thomsen, A. Kumar, T. Pham, A. M. Blackburn, P. Anikeeva, P. Narang, J. M. LeBeau, and F. M. Ross, Nat. Commun. **12**, 1290 (2021).
[31] B. Shi, P. Qi, M. Jiang, Y. Dai, F. Lin, H. Zhang, and Z. Fang, Mater. Adv. **2**, 5542 (2021).
[32] R. V. Gorbachev, I. Riaz, R. R. Nair, R. Jalil, L. Britnell, B. D. Belle, E. W. Hill, K. S. Novoselov, K. Watanabe, T. Taniguchi, A. K. Geim, and P. Blake, Small **7**, 465 (2011).
[33] Ch. Androulidakis, E. N. Koukaras, M. Poss, K. Papagelis, C. Galiotis, and S. Tawfick, Phys. Rev. B **97**, 241414 (2018).
[34] R. E. J. Watkins, P. Rockett, S. Thoms, R. Clampitt, and R. Syms, Vacuum **36**, 961 (1986).
[35] M. M. Haidari, H. Kim, J. H. Kim, M. Park, H. Lee, and J. S. Choi, Sci. Rep. **10**, 8258 (2020).
[36] S. Y. Zhou, G.-H. Gweon, A. V. Fedorov, P. N. First, W. A. de Heer, D.-H. Lee, F. Guinea, A. H. Castro Neto, and A. Lanzara, Nat. Mater. **6**, 770 (2007).
[37] Y. Yan, S. Ding, X. Wu, J. Zhu, D. Feng, X. Yang, and F. Li, RSC Adv. **10**, 39455 (2020).
[38] Z. Zhang, L. Li, J. Horng, N. Z. Wang, F. Yang, Y. Yu, Y. Zhang, G. Chen, K. Watanabe, T. Taniguchi, X. H. Chen, F. Wang, and Y. Zhang, Nano Lett. **17**, 6097 (2017).
[39] M. Liu, Y. Zhuo, A. Sarycheva, Y. Gogotsi, M. A. Bissett, R. J. Young, and I. A. Kinloch, ACS Appl. Mater. Interfaces **14**, 10681 (2022).
[40] C. Martella, C. Massetti, D. S. Dhungana, E. Bonera, C. Grazianetti, and A. Molle, Adv. Mater. 2211419 (published online) (2023).
[41] I. M. Datye, A. Daus, R. W. Grady, K. Brenner, S. Vaziri, and E. Pop, Nano Lett. **22**, 8052 (2022).
[42] M. Veithen, X. Gonze, and Ph. Ghosez, Phys. Rev. B **71**, 125107 (2005).
[43] X. Gonze, B. Amadon, P. M. Anglade, J. M. Beuken, F. Bottin, P. Boulanger, F. Bruneval, D. Caliste, R. Caracas, M. Côté, T. Deutsch, L. Genovese, Ph. Ghosez, M. Giantomassi, S. Goedecker, D. R. Hamann, P. Hermet, F. Jollet, G. Jomard, S. Leroux, M. Mancini, S. Mazevet, M. J. T. Oliveira, G. Onida, Y. Pouillon, T. Rangel, G. M. Rignanese, D. Sangalli, R. Shaltaf, M. Torrent, M. J. Verstraete, G. Zerah, and J. W. Zwanziger, Comput. Phys. Commun. **180**, 2582 (2009).
[44] S. Baroni, S. de Gironcoli, A. Dal Corso, and P. Giannozzi, Rev. Mod. Phys. **73**, 515 (2001).


11 January 2024 11:49:08


© Author(s) 2023